letters to nature

well as through the large-field-gradient positions just above and below the crown-ether molecules.

We have also made direct measurements of the ionic conductivity of the crown-ether salt and also of reference materials. We used an electron-blocking method, in which a compacted disk of the material under test was sandwiched between Li^+/polyethylene oxide disks which were pressed onto Li metal electrodes. The ionic conductivity of (PEG)-$Li(CF_3SO_3)$, where PEG is polyethylene glycol, was measured to be 1.6×10^{-6} S cm^{-1} at 60 °C, in good agreement with literature values[15]. We measured values, also at 60 °C, for a range of $Ni(dmit)_2$ salts: 3×10^{-6} S cm^{-1} for $Li_{0.6}$ (15-crown-5-ether) $[Ni(dmit)_2]_2 \cdot H_2O$; 2×10^{-8} S cm^{-1} for $(C_{16}H_{33})_2(CH_3)_2N[Ni(dmit)_2]$; and 3×10^{-7} S cm^{-1} for $(TPP)[Ni(dmit)_2]_3$, where TPP is tetraphenylphosphonium. Each measurement was made after the current reached its saturated value, typically between 30 and 60 minutes after application of the constant voltage. We have checked that there is no decomposition (for example, water loss) at 60 °C (by thermal gravimetry), and consider that the value of ionic conductivity for the crown-ether Li^+ salt indicates clearly that there is significant Li^+ mobility in this material at this temperature. We have measured significantly lower values in the (electronically insulating) tetra-alkyl ammonium salt and the (electronically conducting) tetraphenylphosphonium salt.

We consider that the electron dynamics on the $Ni(dmit)_2$ chains are controlled by the dynamics of the Li^+ ions in the crown-ether columns. Above 250 K the Li^+ ions are mobile, and do not localize the conduction electrons on the $Ni(dmit)_2$ stacks, which therefore show metallic properties. Between 250 and 200 K the Li^+ ions become immobilized, and provide static coulombic pinning potentials for the conduction electrons on the $Ni(dmit)_2$ stacks, causing localization and the magnetic insulator properties evident in Figs 2 and 3. A metal–insulator transition driven by interaction between ions and electrons in this way is unusual, and the example that we have illustrated here may provide insights into transport properties of other mixed ionic/electronic conductors, such as the conjugated polymer blends recently used by Pei *et al.*[5] in electroluminescent diodes.

The electron-transport system with ion channels that we describe here may allow for the design of electron–cation transport systems for use in active and selective ion transport. For example, a double carrier process could be realised in a redox gradient where the coupled parallel transport of electrons and alkali-metal cations takes place[16]. □

1. Jérome, D. The physics of organic superconductors. *Science* **252,** 1509–1515 (1991).
2. Williams, J. M. *et al.* Organic superconductors—new benchmarks. *Science* **252,** 1501–1508 (1991).
3. Takahashi, T. *et al.* Solid-state ionics—recent trends and future expectations. *Bull. Electrochem.* **11,** 1–33 (1995).
4. Fauteux, D., Massucco, A., Mclin, M., Vanburen, M. & Shi, J. Lithium polymer electrolyte rechargeable battery. *Electrochim. Acta* **40,** 2185–2190 (1995).
5. Pei, Q., Yu, G., Zhang, C., Yang, Y. & Heeger, A. J. Polymer light-emitting electrochemical cells. *Science* **269,** 1086–1089 (1995).
6. Pregel, M. J., Jullien, L. & Lehn, J. M. Towards artificial ion channels—transport of alkali-metal ions across liposomal membranes by bouquet molecules. *Angew. Chem. Int. Edn Engl.* **31,** 1637–1640 (1992).
7. Ghadiri, M. R., Granja, J. R. & Buehler, L. K. Artificial transmembrane ion channels from self-assembling peptide nanotubes. *Nature* **369,** 301–304 (1994).
8. Cassoux, P. *et al.* Molecular-metals and superconductors derived from metal-complexes of 1,3-dithiol-2-thione-4,5-dithiolate (dmit). *Coord. Chem. Rev.* **110,** 115–160 (1991).
9. Kim, H., Kobayashi, A., Sasaki, Y., Kato, R. & Kobayashi, H. New radical-anion complex, $[(CH_3)_4N][Ni(dmit)_2]_2$ with metal-semimetal phase-transition. *Chem. Lett.* 1799–1802 (1987).
10. Guy, D. R. P. & Friend, R. H. Temperature measurement in high pressure cells using a rhodium + 0.5% iron versus chromel thermocouple pair. *J. Phys. E* **19,** 430–433 (1986).
11. Murata, K. *et al.* Superconductivity with the onset at 8 K in the organic conductor beta-(BEDT-TTF)$_2$I$_3$ under pressure. *J. Phys. Soc. Jpn* **54,** 1236–1239 (1985).
12. Estes, W. E., Gavel, D. P., Hatfield, W. E. & Hodgson, D. J. Magnetic and structural characterisation of dibromo- and dichlorobis(thiazole) copper(II). *Inorg. Chem.* **17,** 1415–1421 (1978).
13. Obertelli, S. D., Friend, R. H., Talham, D. R., Kurmoo, M. & Day, P. Magnetic susceptibility and EPR of the Organic conductors α′-(BEDT-TTF)2X, X=AuBr$_2$, CuCl$_2$ and Ag (CN)$_2$. *J. Phys. Cond. Matter* **1,** 5671–5680 (1989).
14. Cohen, M. H. & Reif, F. in *Solid State Physics* (eds Seitz, F. & Turnbull, D.) 321–438 (Academic, New York, 1957).
15. Robitaille, C. D. & Fauteux, D. Phase-diagrams and conductivity characterization of some PEO-Li$_x$ electrolytes. *J. Electrochem. Soc.* **133,** 315–325 (1986).
16. Grimaldi, J. J. & Lehn, J. M. Multicarrier transport: coupled transport of electrons and metal cations

mediated by an electron carrier and a selective cation carrier. *J. Am. Chem. Soc.* **101,** 1333–1334 (1979).
17. Burla, M. C. *et al.* SIR88—a direct-methods program for the automatic solution of crystal-structures. *J. Appl. Crystallogr.* **22,** 389–393 (1989).

Magnitudes of sea-level lowstands of the past 500,000 years

E. J. Rohling*, **M. Fenton***, **F. J. Jorissen**†, **P. Bertrand**†, **G. Ganssen**‡ & **J. P. Caulet**§

* *Department of Oceanography, Southampton University, Southampton Oceanography Centre, Southampton SO14 3ZH, UK*
† *Département de Géologie et Océanographie, Université de Bordeaux I, CNRS URA 197, Avenue des Facultés, 33405 Talence Cedex, France*
‡ *Department of Earth Sciences, Free University Amsterdam, De Boelelaan 1085, 1081 HV Amsterdam, The Netherlands*
§ *Laboratoire de Géologie, National Museum for Natural History, CNRS URA 723, 43 Rue Buffon, 75005 Paris, France*

Existing techniques for estimating natural fluctuations of sea level and global ice-volume from the recent geological past exploit fossil coral-reef terraces or oxygen-isotope records from benthic foraminifera. Fossil reefs reveal the magnitude of sea-level peaks (highstands) of the past million years, but fail to produce significant values for minima (lowstands) before the Last Glacial Maximum (LGM) about 20,000 years ago, a time at which sea level was about 120 m lower than it is today[1–4]. The isotope method provides a continuous sea-level record for the past 140,000 years (ref. 5) (calibrated with fossil-reef data[6]), but the realistic uncertainty in the sea-level estimates is around ±20 m. Here we present improved lowstand estimates—extending the record back to 500,000 years before present—using an independent method based on combining evidence of extreme high-salinity conditions in the glacial Red Sea with a simple hydraulic control model of water flow through the Strait of Bab-el-Mandab, which links the Red Sea to the open ocean. We find that the world can glaciate more intensely than during the LGM by up to an additional 20-m lowering of global sea-level. Such a 20-m difference is equivalent to a change in global ice-volume of the order of today's Greenland and West Antarctic ice-sheets.

Our technique relies on evidence of adverse living conditions for planktonic foraminifera in the glacial Red Sea due to extremely high salinities, giving rise to so-called 'aplanktonic' zones. These contain only few specimens (mostly *Globigerinoides ruber*) and are found not only in our core MD921017 (Fig. 1), but throughout the Red Sea[7–11]. Planktonic pteropods[10] and benthic foraminiferal faunas were less affected, although the latter show increased abundances of high-salinity-resistant miliolid taxa (Fig. 1e; also refs 8, 9). Inorganic aragonite coatings, cements and concretions indicative of high salinities are found within the 'aplanktonic' zones of stages 2, 6 and 12 (Fig. 1b), in agreement with previous reports[12,13]. Multi-disciplinary studies of the youngest aplanktonic zone (LGM) indicate that Red Sea salinities rose to 50 ± 2 practical salinity units (p.s.u.), that is, 10 ± 2 p.s.u. higher than in the adjacent ocean[9,10,14]. The highest estimate[11] is 55 p.s.u. Similar faunal reductions and compositional changes, as well as distinct aragonite

occurrences, characterize the stage 6 and 12 glacial maxima, reflecting comparable high-salinity conditions (Fig. 1). Continuation of a more diverse, although severely reduced, fauna through stages 10 and 8 suggests less harsh conditions, with those during stage 8 being least restricted.

Arguments for hydraulic control of flow through the Strait of Bab-el-Mandab (SBM) and conservation of mass and salt[14,15] demonstrate that the glacial freshwater deficit was similar to the present ($2 \, \mathrm{m \, yr^{-1}}$), and that the high salinities resulted from restricted marine exchange through the SBM, which today is only 137 m deep[16]. Continuation of benthic faunas, albeit in reduced numbers and different compositions, indicates that all glacial sea-level drops of the past 500 kyr left sufficient communication between the Red Sea and the open ocean to prevent worse salinization and consequent sterilization (Fig. 1c, e). The calculations[14,15] may be rearranged to find the 'critical' glacial sill depth (H_{crit}) at which salinities would rise to reconstructed LGM values, and so trigger an aplanktonic interval. We use the more common range of estimates for LGM salinities[9,10,14], with a salinity difference (ΔS) across the SBM of 10 ± 2 p.s.u., and in sensitivity tests with $\Delta S = 15$ p.s.u. and $\Delta S = 10 \pm 5$ p.s.u. we evaluate the potential effects of the highest-salinity extreme[11].

A glacial water deficit of $2.0 \pm 0.5 \, \mathrm{m \, yr^{-1}}$ is used, allowing for uncertainties in sea–air temperature contrasts and freshwater input of a factor of two, and $\pm 2 \, \mathrm{m \, s^{-1}}$ uncertainty in mean wind speed variations[14]. As glacial exposure of shelves would reduce the Red Sea surface area by 50%, volumes of net glacial evaporation (= area × deficit) amounted to 0.50 ± 0.13 times present-day values. Hydraulic control defines $Q = W0.375H_{\mathrm{crit}}(0.375H_{\mathrm{crit}}7.4 \times 10^{-3}\Delta S)^{0.5}$ for the maximum exchange solution, while $Q = (3.29\gamma Q_{\mathrm{p}})/\Delta S$ follows from conservation of mass and salt[14,15]. Here Q is volume of Red Sea outflow, W is the glacial width of the shallow passage of the SBM, and γ is the ratio of glacial to present-day net evaporation; subscript p indicates present-day value.

Consequently, $H_{\mathrm{crit}} = 18 \pm 5$ m, for $\Delta S = 10 \pm 2$ p.s.u., $W = 11 \pm 1$ km, $\gamma = 0.50 \pm 0.13$ and $Q_{\mathrm{p}} = 0.32 \pm 0.03$ Sv (1 Sv = $10^6 \, \mathrm{m^3 \, s^{-1}}$)[14–17]. Potentially increased mixing of inflow and outflow for reduced sill depths favours values of H_{crit} towards the higher end of its confidence interval over those towards the lower end. We combine the present-day sill depth of 137 m with H_{crit} to estimate past sea-level lowstands, but we first evaluate whether—and to what extent—correction is needed for uplift in the SBM region.

Total planktonic foraminiferal abundances show a distinct decrease over the interglacial periods of the past 500 kyr in core MD921017 (Figs 1b, 2a). A similar trend is seen for the past 380 kyr contained in nearby core KL11[11]. Sedimentation rates throughout MD921017 are very uniform (see Supplementary Information), so that foraminiferal numbers per gram—based on constant sample thickness—closely approximate true fluxes per unit time.
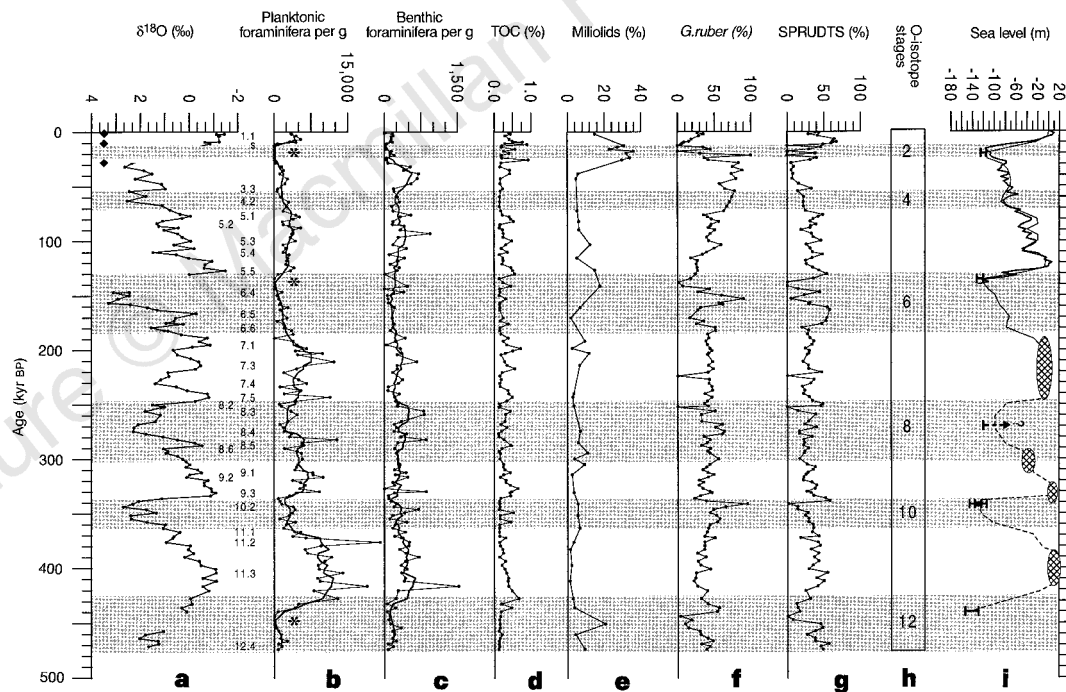

Figure 1 Results for core MD921017, Red Sea (19° 23′ 24″ N, 38° 40′ 84″ E, water depth 570 m). All variables plotted against time in calendar years (kyr BP) according to correlation with SPECMAP[22]. **a**, Oxygen-isotope record (versus PDB standard) for *Globigerinoides ruber* in the 250–350 μm size fraction (filled circles). Numbers refer to SPECMAP events[22]; filled diamonds indicate samples used for AMS radiocarbon dating (1,666 ± 26, 9,681 ± 41 and 25,300 ± 200 radiocarbon years BP, respectively). **b**, Planktonic foraminifera per gram dry weight (thin line). Asterisks highlight true aplanktonic zones of oxygen isotope stages 2, 6 and 12 which contain aragonitic coatings, cement and nodules. Heavy line is five-point moving-average highlighting the general trends. **c**, Benthic foraminifera per gram dry weight (thin line), with five-point moving average (heavy line). We note factor 10 difference between scales in **b** and **c**. **d**, Down-core variation in TOC (%) (LECO 125-CS elemental analyser). Preparation involved removal of carbonate by acidification using dilute hydrochloric acid. **e**, Abundance of miliolids relative to total benthic foraminiferal fauna. Although of lower resolution than the other records, the miliolid percentages do show a general increase in abundance through the record, as well as peaks associated with the aplanktonic zones. **f**, Abundance of *Globigerinoides ruber* relative to total planktonic foraminiferal fauna. **g**, Abundance of SPRUDTS group relative to total planktonic foraminifera. This group represents a cluster of the individually infrequent subtropical species *Globigerinoides sacculifer*, *Hastigerina pelagica*, *Globoturborotalia rubescens*, *Orbulina universa*, *Globigerina digitata*, *Globoturborotalia tenella* and *Globigerinella siphonifera*[18]. **h**, Oxygen isotope stages[22]. **i**, Global sea level record. The heavy solid line through the past 140 kyr is based on benthic isotopes[5] and the thin solid line through the past 200 kyr is based on coral reef terraces and benthic isotopes[4]. Cross-hatched ovals show reported ranges of interglacial sea-level highstands[2–4,21]. Thick error bars in stages 2, 6, 8, 10 and 12 represent ranges of glacial sea-level lowstands according to the model presented here. The dashed line through stages 8–12 shows schematic sea-level fluctuations sketched through the control points following the main trends in the oxygen-isotope record.

Consequently, the decreasing trend in planktonic foraminiferal numbers reflects: (1) a steady decrease in interglacial productivity over the past 500 kyr; or (2) a progressive deterioration of living conditions for foraminifera through increasing isolation of the Red Sea from the open ocean.

Investigation of other parameters for interglacial periods, to detect long-term changes unrelated to glacial cycles, provides no support for the first option. First, the total organic carbon (TOC) record shows only minor, random fluctuations (Fig. 1d). Second, there are no long-term trends in the carbon isotope record. Third,
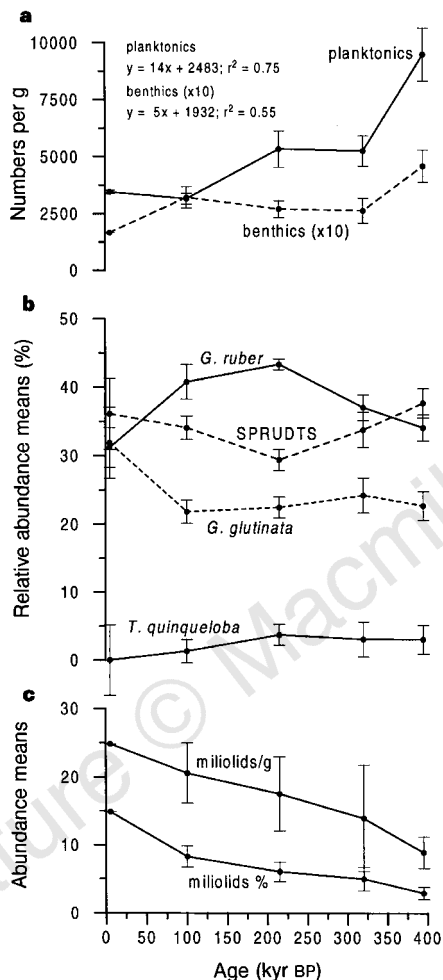
the continuously low-diversity planktonic foraminiferal faunas are totally dominated by relative fluctuations (within a 100% sum) of only two taxonomic groups, *G. ruber* and the SPRUDTS group (see Fig. 1 legend for details), both of which are typical of warm and oligotrophic conditions[18] (Figs 1f, g, 2b). Last, there is only a weak, statistically insignificant, trend in total benthic foraminiferal abundances, whereas a significant decrease would be expected under conditions of decreasing primary/export productivity (= food supply) (Figs 1c, 2a).

The second option—increasing Red Sea 'restriction'— is supported by a steady increase in the abundances of high-salinity resistant[8,9] miliolid species in the benthic foraminiferal fauna over the interglacial periods of the past 500 kyr (Figs 1e, 2c). The increasing restriction would have occurred within a context of already limited exchange with the open ocean, as witnessed by: the lack of successful[19] 'invasions' into the Red Sea by oceanic species like *Globigerina bulloides*, *Globorotalia menardii* and *Neogloboquadrina dutertrei*; the limited and diminishing presence of *Turborotalita quinqueloba* (Fig. 2b) (these four species abound just outside the SBM in core MD921005; 11° 35′ 13″ N, 43° 31′ 84″ E); and the amplified glacial–interglacial contrasts throughout the Red Sea oxygen-isotope record relative to those of the open ocean (Fig. 1a), a typical characteristic of evaporative marginal basins related to their restriction from the world ocean. The inferred slow but progressive isolation of the Red Sea, superimposed on already restricted communication with the open ocean, is best explained by slow and fairly continuous uplift of a shallow sill.

The rate of uplift may be assessed using the present-day sill depth of 137 m (ref. 16) and previous estimates that sea level stood around 125 m below present sea level (b.p.s.l.) during stage 6 (135 kyr BP) (Fig. 1i)[4,5]. Addition of H_{crit} gives an estimated stage 6 sill depth of 143 m b.p.s.l., which implies 6 m uplift in 135 kyr (4.4 cm kyr^{-1}). This rate is a factor of 5–10 smaller than the assumed constant rates of classical reef-terrace-based sea-level studies[1–4]. To account for uncertainties in the derivation of the rate and/or its possible temporal nonlinearities, a 50% confidence interval is added, giving 0.044 ± 0.022 m kyr^{-1}. Our model then back-calculates the stage 6 sea level drop at $137 + (135 \times 0.044) - H_{crit} = 125$ m, with a confidence interval of ± 6 m based on propagation[20] of uncertainties in H_{crit} (± 5 m) and uplift rate (± 0.022 m kyr^{-1}). Validation of the model through determination of the LGM

Figure 2 Trends through interglacial stages. **a**, Trends in the numbers of planktonic and benthic foraminifera per gram sediment dry weight, through interglacial stages 11, 9, 7, 5 and 1. Positions on age axis are simple stage mid-points. Stage 3 is excluded as this in fact is a warm interstadial within the last glacial period. Symbols indicate mean values, and error bars an interval of ± 1 standard error of the mean. Benthic numbers have been multiplied times 10, to allow plotting on the same scale as planktonic numbers. Equations and r^2 coefficients concern linear fits through the two records. Linear fit for planktonics shows a significant trend ($\alpha = 0.05$), for benthics the trend is weak and statistically insignificant. We emphasise that, as stage 1 is continuing, its values may be less representative than those of the other (completed) interglacial periods. **b**, Mean relative abundances of *Globigerinoides ruber* and SPRUDTS-group (see also Fig. 1), and of *Globigerinita glutinata* and *Turborotalita quinqueloba*, in percentages relative to total planktonic foraminiferal fauna, through interglacial stages 11, 9, 7, 5 and 1. Symbols, error bars and note on stage 3 and 1 values as in **a**. **c**, Trends in high-salinity indicative mioliolid benthic foraminifera–both relative to total benthic foraminiferal faunta (%), and as absolute abundances (numbers per gram dry weight)–through interglacial stages 11, 9, 7, 5 and 1. Symbols, error bars and note on stage 3 and 1 values as in **a**.
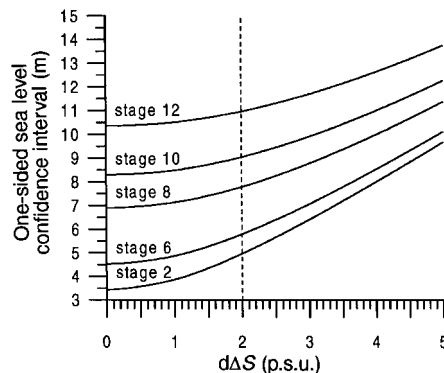

Figure 3 Sensitivity of confidence interval. Changes in the confidence intervals around the reconstructed mean sea level lowstands for glacial stages, 2, 6, 8, 10 and 12, for glacial Red Sea salinity contrast $\Delta S = 10$ p.s.u. $\pm$ a variable confidence interval dΔS. Effects are investigated per glacial stage for a range of dΔS values from 0 to 5 p.s.u. Dashed line indicates d$\Delta S = 2$ as used in this Letter. The sea level confidence intervals (y axis) essentially change due to modification of the confidence interval around H_{crit}, which by close approximation corresponds to the line marked "stage 2".

(20 kyr BP) sea-level lowstand gives 120 ± 5 m, in agreement with fossil reef results[1] and supporting our mean value for H_{crit}.

To evaluate the dependence of our lowstand reconstructions on the main assumption that previous glacial ΔS values were similar to LGM values of 10 ± 2 p.s.u., we perform two tests based on the highest extreme glacial salinity estimate (55 p.s.u.; ref. 11). One increases ΔS to 15 p.s.u.; the other keeps ΔS at 10 p.s.u. but increases its confidence interval ($d\Delta S$) from ± 2 to ± 5 p.s.u. In the first test, H_{crit} is smaller, and reconstructed sea level drops are greater, by a maximum of 6 m. In the second test, with $d\Delta S$ increased by a factor of 2.5, the lowstand confidence intervals remain accurate within a factor of 2 (Fig. 3). These results justify the use of the SBM uplift rate with H_{crit} to study pre-stage-6 lowstands, noting that our method is more likely to underestimate rather than overestimate past sea-level drops, by a few metres.

Accounting for uplift since stage 8 (270 kyr BP), sill depth was around 150 m b.p.s.l. Stage 8 does not contain a completely 'aplanktonic' interval. Although the total planktonic foraminiferal numbers are strongly reduced, the main species composition shows little change that might reflect high-salinity stress (Fig. 1). We infer that sill depth remained considerably greater than H_{crit}. To allow continuation of all observed planktonic species, Red Sea salinity should have remained below a maximum of ~45 p.s.u., requiring a minimum sill depth of ~30 m (compare ref. 14). Hence, the maximum conceived stage 8 sea level drop is $150 - 30 = 120$ m b.p.s.l.(± 8 m).

A similar argument to that for stage 8 may be made for stage 10 (340 kyr BP). However, stage 10 shows a much closer approximation of a complete 'aplanktonic' zone, with disruption of the main species composition. We infer that sill depth was maintained between H_{crit} (18 m) and 30 m, defining a stage 10 lowstand between 134 and 122 m b.p.s.l. (± 9 m).

Stage 12 (440 kyr BP) contains a true 'aplanktonic' zone (Fig. 1), suggesting a sill depth around H_{crit} and, consequently, a sea-level lowstand of 139 m b.p.s.l. (± 11 m). This mean value implies that global ice-volume during stage 12 exceeded LGM values by some 15%. This independently derived result validates the only previous estimate of stage 12 ice-volume, based on benthic oxygen-isotope records[5].

Our lowstand values allow assessment of sea-level rises during the main deglaciations of the past 500 kyr (Fig. 1i), for comparison with that of 120 m following the LGM[1]. With the maximum stage 5 sea level ~6 m above the present[2,6], the stage 6–5 sea-level rise was around 131 ± 6 m. During interglacial stage 7, sea level remained below the present-day level[4,5], giving a maximum amplitude for the stage 8–7 sea-level rise of 120 m, although the actual rise was probably considerably smaller. The stage 9 highstand reached 0–15 m above the present-day level[4,5], giving a stage 10–9 sea-level rise between 122 and 149 m. The largest sea-level rise of the past 500 kyr followed the stage 12 lowstand of 139 ± 11 m b.p.s.l. and culminated in a maximum stage 11 highstand up to 20 m above present-day sea level[21].

We conclude that the last glacial–interglacial cycle showed ice-volume fluctuations that were more than 10% smaller than those that occurred in three out of four of the immediately preceding main cycles. The stage 12–11 sea level rise implies that over 30% greater ice-volume changes were involved in Quaternary glacial–interglacial cycles than would be expected on the basis of the last cycle alone. □

1. Fairbanks, R. G. A 17,000 year glacio-eustatic sea level record: Influence of glacial melting rates on the Younger-Dryas event and deep ocean circulation. *Nature* **342**, 637–642 (1989).
2. Radtke, U. & Grün, R. Revised reconstruction of middle and late Pleistocene sea-level changes based on new chronologic and morphologic investigations in Barbados, West Indies. *J. Coastal Res.* **6**, 699–708 (1990).
3. Pirazzoli, P. A. *et al.* A one million-year-long sequence of marine terraces on Sumba Island, Indonesia. *Mar. Geol.* **109**, 221–236 (1993).
4. Bard, E. *et al.* Pleistocene sea levels and tectonic uplift based on dating of corals from Sumba Island, Indonesia. *Geophys. Res. Lett.* **23**, 1473–1476 (1996).
5. Shackleton, N. J. Oxygen isotopes, ice volume and sea level. *Quat. Sci. Rev.* **6**, 183–190 (1987).
6. Chappell, J. & Shackleton, N. J. Oxygen isotopes and sea level. *Nature* **324**, 137–140 (1986).
7. Berggren, W. A. & Boersma, A. in *Hot Brines and Heavy Metal Deposits* (eds Degens, E. T. & Ross, D. A.) 282–298 (Springer, 1969).
8. Halicz, E. & Reiss, Z. Palaeoecological relations of foraminifera in a desert enclosed sea—The Gulf of Aqaba. *Mar. Ecol.* **2**, 15–34 (1981).
9. Locke, S. & Thunell, R. C. Palaeoceanographic record of the last glacial-interglacial cycle in the Red Sea and Gulf of Aden. *Palaeogeogr. Palaeoclimatol. Palaeoecol.* **64**, 163–187 (1987).
10. Almogi-Labin, A., Hemleben, C., Meischner, D. & Erlenkeuser, H. Palaeoenvironmental events during the last 13,000 years in the central Red Sea as recorded by pteropoda. *Paleoceanography* **6**, 83–98 (1991).
11. Hemleben, C. *et al.* Three hundred and eighty thousand year long stable isotope and faunal records from the Red Sea: Influence of global sea level change on hydrography. *Paleoceanography* **11**, 147–156 (1996).
12. Milliman, J. D., Ross, D. A. & Ku, T. L. in *Hot Brines and Heavy Metal Deposits* (eds Degens, E. T. & Ross, D. A.) 724–736 (Springer, New York, 1969).
13. Ku, T. L., Thurber, D. L. & Mathieu, G. G. in *Hot Brines and Heavy Metal Deposits* (eds Degens, E. T. & Ross, D. A.) 348–359 (Springer, New York, 1969).
14. Rohling, E. J. Glacial conditions in the Red Sea. *Paleoceanography* **9**, 653–660 (1994).
15. Rohling, E. J. & Zachariasse, W. J. Red Sea outflow during the last glacial maximum. *Quat. Int.* **31**, 77–83 (1996).
16. Werner, F. & Lange, K. A bathymetric survey of the sill area between the Red Sea and Gulf of Aden. *Geol. Jahrb. D* **13**, 125–130 (1975).
17. Siedler, G. in *Hot Brines and Heavy Metal Deposits* (eds Degens, E. T. & Ross, D. A.) 131–137 (Springer, New York, 1969).
18. Rohling, E. J., Jorissen, F. J., Vergnaud-Grazzini, C. & Zachariasse, W. J. Northern Levantine and Adriatic Quaternary planktic foraminifera; Reconstruction of paleoenvironmental gradients. *Mar. Micropaleontol.* **21**, 191–218 (1993).
19. Ganssen, G. & Kroon, D. Evidence for Red Sea surface circulation from oxygen isotopes of modern surface waters and planktonic foraminiferal tests. *Paleoceanography* **6**, 73–82 (1991).
20. Squires, G. L. *Practical Physics* 3rd edn (Cambridge Univ. Press, 1988).
21. Howard, W. R. A warm future in the past. *Nature* **388**, 418–419 (1997).
22. Imbrie, J. *et al.* in *Milankovitch and Climate* (eds Berger, A. *et al.*) 269–305 (Reidel, Hingham, MA, 1984).

Megaripple migration in a natural surf zone

Edith L. Gallagher*, Steve Elgar† & Edward B. Thornton*

* *Oceanography Department, Naval Postgraduate School, Monterey, California 93943, USA*
† *School of Electrical Engineering and Computer Science, Washington State University, Pullman, Washington 99164, USA*

Migrating megaripples are bedforms that appear in the surf zone of sandy coasts[1]. With heights of 0.1–0.5 m and wavelengths of 1–5 m, they are similar in size and shape to small dunes, large ripples, or sand waves. Such sedimentary bedforms have been studied in subaerial[2], steady-flow[3] and intertidal[4] environments, as well as in laboratory flume experiments[5]. They affect overlying currents by introducing hydraulic roughness[4,6], and may provide a mechanism for sediment transport[7,8] as well as forming sedimentary structures in preserved facies[9,10]. The formation, orientation and migration of such bedforms is not understood well[11,12]. Dunes, for example, can be aligned with their crests perpendicular to steady unidirectional winds[13], but in more complex wind fields their orientation becomes difficult to predict[14–17]. Similarly, it is not known how sea-floor megaripples become aligned and migrate in the complex flows of the surf zone. Here we present observations in the surf zone of a natural beach which indicate that megaripples do not migrate in the direction of the vector sum of the currents, but are aligned so that the sediment transport normal to the bedform crest is maximized[17]. This may need to be taken into account in modelling morphology change and interpreting existing and fossil morphologic patterns.